J Mater Sci (2010) 45:3350–3366
DOI 10.1007/s10853-010-4356-0

Static and dynamic characterization of composition cork for sandwich beam cores

R. A. S. Moreira · F. J. Q. de Melo · J. F. Dias Rodrigues

Received: 11 November 2009 / Accepted: 25 February 2010 / Published online: 23 March 2010

Abstract Composition cork can be regarded as an interesting solution for light-damped sandwich panels. Despite the emergent interest on these materials for structural applications, there is a lack of information concerning its static and dynamic properties. This study presents a comparative study on a set of different experimental characterization methodologies applied on a selected agglomerated cork for vibration damping applications. The obtained results support the assumption of an air spring/viscous-based mechanism ruling the low-frequency behaviour of these materials. This assumed behaviour is a result from the observations of the cellular microstructure of natural and composition corks. Indicative values for the *Young*'s modulus, storage modulus and loss factor are provided as results from this study. In addition, a multilayer beam finite element, based on a mixed formulation, is proposed to be applied in an inverse characterization methodology and to be used also for the experimental validation tasks. The finite element proved to be efficient and accurate.

Introduction

Composite materials have been widely used in state-of-the-art structural applications, such as in the automotive, aeronautical and aerospace structural engineering fields, providing interesting and valuable stiffness/mass ratios, where they have been responsible for important progresses in design enhancement, safety and durability improvement and cost reduction, either in terms of manufacturing or operation and maintenance. The valuable performance of laminate composite structures in static or dynamic condition applications has motivated a continuous development on new materials and laminate configurations, improved and cost-effective manufacturing processes and, specially, on more efficient modelling and design methods.

An interesting laminate configuration, usually referred to as sandwich panel, combines the high stiffness of the external layers with an adequate internal core, which, for instance, can be deliberately designed to provide a significant material damping capability. Such configuration enables an interesting combination of a highly resistant material applied in the skins and a core material able to dissipate large amounts of energy, usually as heat, thus reducing the structure vibration energy, which provides an efficient and inherent passive dynamic control. Such laminate materials have been gradually applied in some high-end and critical structures, like aeronautic components, aerospace frames and panels, among other justifiable applications. However, the continuous need for safer, quieter, reliable and cost-effective structures has motivated the structural design community, especially those acting on the transportation field, to face these damped sandwich structures as promising solutions to succeed towards this goal.

Soft elastomers with a high loss factor are the materials mostly applied in surface or sandwich damping treatments [1–3]. Despite offering a reduced mass and an important damping capability, the success of the application of these materials is often diminished when required to operate under a wide working temperature range. In such a case, it is impossible to design an effective single-layer damping

R. A. S. Moreira (✉) · F. J. Q. de Melo
Departamento de Engenharia Mecânica, Universidade de Aveiro, Campus Santiago, 3810-193 Aveiro, Portugal
e-mail: rmoreira@ua.pt

J. F. Dias Rodrigues
Faculdade de Engenharia da Universidade do Porto, R. Dr. Roberto Frias, 4050-465 Porto, Portugal

treatment of sandwich panel, becoming necessary to create a large assembly of several viscoelastic materials providing different transition temperatures to accomplish the entire temperature range [4]. Moreover, the uppermost temperature limit of these structures is usually low, due to the material degradation process, which rules out the use of these damping solutions in high-temperature applications, like exhaust systems, engine parts, or even parts that, working at room temperatures, are intensively heated by the sunlight, like automotive roof panels.

Recently, the use of natural cork, or more precisely specially formulated composition corks, has been regarded as a promising solution for damping cores in sandwich constructions [5], providing a useful damping capacity over a broad temperature range. In addition, these materials present an extensive set of interesting capabilities, like its low weight, approximately one-tenth of the one presented by viscoelastic materials, its high chemical resistance, and, especially, its broadly acclaimed thermal insulation and acoustic attenuation characteristics, with noteworthy impact in automotive and aeronautical applications. Furthermore, composition corks are easily formulated to attain a specific and homogeneous set of properties and can be easily machined or cut. Since for some countries this material plays an important role in export budget, there is a growing effort to enlarge its application field.

The assessment of the damping characteristics of composition cork applied in the core of sandwich beams has been investigated by Dias Rodrigues and Moreira [6], considering these materials as frequency-dependent viscoelastic materials. Experimental material characterization studies [5] suggest the suitability of such generalized hysteretic damping constitutive model. However, the regular cellular structure of the cork, presenting partially closed cells, as well as the irregular macro granular structure of the agglomerate, proposes the possibility of a considerable contribution from a viscous damping mechanism onto the global damping capability, with special relevance for the low frequency range.

Experimental characterization data for natural and composition corks is limited to a small set of published studies [7–17]. Furthermore, since composition corks are available in the market in a wide range of material formulations, with variations on the cork grain size, cork density, agglomerate density and adhesive material, a reference for composition cork properties is not available in the literature or in material databases. In this study, both static and dynamic characterization procedures are applied to define a reference value interval for the complex modulus of a selected composition cork material (Ref. 8003—see Appendix), which proved to be a promising solution for structural passive damping solutions [5, 6].

In addition to the material constitutive model issues, the numerical simulation of sandwich structures—in this particular case, shear deformable beams—requires also a representative spatial model able to account for the skin/core interrelation, especially when these parts present a high modulus ratio. For such modulus ratio conditions, which can reach values higher than 1000:1, the shear deformation pattern to which the core is subjected to represents an important role in the sandwich beam flexural stiffness and damping capacity. For this purpose, layered models [18] and layerwise models [19–21] can be efficiently applied since this modelling approach is based on a piecewise description of the displacement field along the beam/plate thickness direction, allowing the direct prescription of the interlayer displacement continuity conditions. However, this purely displacement layerwise model does not impose directly any constraint for the stress and strain fields distribution, especially under the natural stress and strain interlayer continuity conditions. In this study, a hybrid formulation [22], considering both the displacement and the stress fields, is applied to enable an accurate distribution and prescribed continuity of the stress field along the thickness and between the adjacent layers. An experimental study with sandwich beams with a composition cork core is developed to validate the proposed model and assess the damped sandwich concept with composition cork cores feasibility.

Finite element formulation

The finite element hereby proposed is a laminate beam element in which each generic layer is physically represented by a four node bi-dimensional plane stress finite element. The aim of this finite element formulation is to ensure the continuity of the shear stresses along the sandwich thickness, an issue that is not directly imposed, and thus not really ensured, with the displacement-based solutions.

As described, each individual finite element representing a generic layer of the laminate domain has four corner nodes, where the longitudinal degrees of freedom u_1, u_2, u_3 and u_4 are defined (Fig. 1). Two additional degrees of freedom, the transversal displacements w_i and w_j, are defined for the laminate finite element and are located in a pair of auxiliary nodes, i and j. These nodes do not describe the element geometry and are located at the mid side of vertical edges of the finite element (Fig. 1).

In order to define the entire beam finite element, the set of finite elements representing each individual layer is assembled in the thickness direction considering that the deformation along the thickness direction is negligible, i.e.

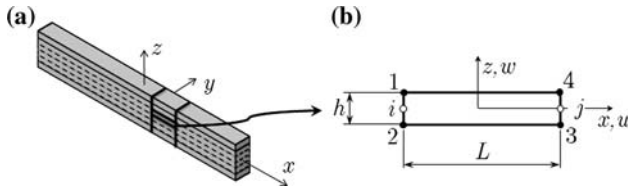

Fig. 1 Four-node beam finite element with two auxiliary nodes (i, j). **a** Beam laminate and **b** generic layer finite element

the w_i and w_j degrees of freedom are shared between all the layer finite elements for the same beam finite element.

When dealing with low order finite elements, the stiffness matrix formulation may suffer from a locking effect (shear or trapezoidal locking). This numerical pathology can be circumvented by using reduced or selective integration [23], which has the drawback of originating a rank deficiency in the stiffness matrix, limiting the finite element performance due to the resulting spurious energy hourglass modes [24]. However, it is possible to render the element free from those instability modes by adopting stabilization methods [24].

In the finite element formulation being proposed, the uncoupled definition for the transverse displacement and the section rotation introduces a constraint in the displacement field and reduces the deformation modes subspace. In addition, and contrary to the uniform reduced integration, the use of the selective integration scheme herein adopted, where only the transverse shear component is evaluated through one integration point, retains the correct rank of the element stiffness, and consequently the rank of the global stiffness matrix [23].

Displacement field

As mentioned, the finite element representing each layer has four corner nodes plus two auxiliary nodes necessary to define a uniform transverse displacement for all the elements or layers along the transverse section. The assumptions considered in the present formulation are synthesized as follows:

- The four corner nodes of the element are used to define only the inplane displacement, u;
- The element is considered to be incompressible along the transverse z-direction;
- The transverse displacement, w, is uniform along coordinate z for each x-constant and is defined by interpolation functions with reference to additional nodes i and j; it is x-coordinate dependent.

With these assumptions, the definition of the displacement field is reported to a problem in plane elasticity where $u(x, z)$ and $w(x)$ are, respectively, the longitudinal and the transverse displacements. The displacement field within the finite element domain is determined using an interpolator operator onto the nodal values as follows:

$$u(x,z) = N_{1x}N_{1z}u_1 + N_{2x}N_{2z}u_2 + N_{3x}N_{3z}u_3 + N_{4x}N_{4z}u_4$$
$$w(x) = N_i w_i + N_j w_j \tag{1}$$

The abovementioned interpolation functions are defined as

$$N_{1z} = N_{4z} = \frac{1}{h}\left(z + \frac{h}{2}\right) \quad N_{1x} = N_{2x} = N_i = -\frac{1}{L}\left(x - \frac{L}{2}\right)$$
$$N_{2z} = N_{3z} = -\frac{1}{h}\left(z - \frac{h}{2}\right) \quad N_{3x} = N_{4x} = N_j = \frac{1}{L}\left(x + \frac{L}{2}\right) \tag{2}$$

where $x \in [-L/2, L/2]$ and $z \in [-h/2, h/2]$, with L and h, respectively, being the length of the finite element and the thickness of the layer (as described in Fig. 1). It is noted that the displacement w only depends upon the x coordinate while u depends on x and z coordinates.

The displacement field described by (1) can be defined in a matrix form as

$$\{\mathbf{u}(x,z)\} = [\mathbf{N}(x,z)]\{d\} \tag{3}$$

where $\{d\}$ represents the generalized displacement vector:

$$\{d\} = \{\, w_i \quad u_1 \quad u_2 \quad w_j \quad u_3 \quad u_4 \,\}^{\mathrm{T}} \tag{4}$$

and the matrix $[\mathbf{N}(x,z)]$ represents the interpolation operator described by the shape functions (2).

Strain field

The strain field of the four-node beam finite element is defined assuming plane stress conditions and linear elastic deformation, as

$$\{\varepsilon(x,z)\} = \begin{Bmatrix} \varepsilon_{xx} \\ \gamma_{xz} \end{Bmatrix} \tag{5}$$

where ε_{xx} and γ_{xz} are, respectively, the normal and the shear strains. The strain field can be obtained by applying the differential operator $[\mathbf{L}]$ onto the displacement field (3) as

$$\{\varepsilon(x,z)\} = [\mathbf{L}][\mathbf{N}(x,z)]\{d\} = [\mathbf{B}(x,z)]\{d\} \tag{6}$$

where $[\mathbf{B}(x,y)]$ is the deformation matrix defined by the membrane and bending strain $\left[\mathbf{B}^{\mathrm{B}}\right]$and shear strain $\left[\mathbf{B}^{\mathrm{S}}\right]$terms.

Stress field

In the finite element under consideration in this study, the stress field is defined independently from the strain field, following a procedure similar to the displacement field

description. Therefore, the stress field inside the finite element domain is interpolated from the nodal stress variables, as

$$\{\sigma(x,z)\} = [\mathbf{N}^{\sigma}(x,z)]\{\sigma\} \tag{7}$$

where the nodal stress vector $\{\sigma\}$ is described by the stress nodal parameters:

$$\{\sigma\} = \{\sigma_{x1}\ \sigma_{x2}\ \sigma_{x3}\ \sigma_{x4}\ \tau_{xz1}\ \tau_{xz2}\ \tau_{xz3}\ \tau_{xz4}\}^{\mathrm{T}} \tag{8}$$

and the stress related interpolation matrix is defined by the set of terms:

$$[\mathbf{N}^{\sigma}(x,z)] = [N_{1x}N_{1z} \quad N_{2x}N_{2z} \quad N_{3x}N_{3z} \quad N_{4x}N_{4z}] \tag{9}$$

using the same interpolation operator applied onto the displacement field.

Variational formulation

After the definition of the displacement, strain and stress fields, the constitutive operator can be applied to describe the stress–strain relation as

$$\{\sigma(x,z)\} = [\mathbf{D}]\{\varepsilon(x,z)\} \tag{10}$$

where $[\mathbf{D}]$ is the elasticity matrix containing the elastic properties of the material (the *Young*'s modulus E and the *Poisson*'s ratio v, or alternatively, the shear modulus G).

An alternative formulation for (10), using the flexibility concept, is

$$[\mathbf{D}]^{-1}\{\sigma(x,z)\} = \{\varepsilon(x,z)\} \tag{11}$$

Following the *Hellinger-Reissner* variational principle [25, 26], the total energy results from the superposition of the elastic strain energy (first term of Eq. 12), the complementary energy (second term of Eq. 12), and the work performed by external forces:

$$\Pi_{\mathrm{P}} = \frac{1}{2}\int_{-L/2}^{L/2}\int_{-h/2}^{h/2}\{\sigma\}^{\mathrm{T}}[\mathbf{D}]^{-1}\{\sigma\}\,\mathrm{d}x\mathrm{d}z - \int_{-L/2}^{L/2}\int_{-h/2}^{h/2}\{\sigma\}^{\mathrm{T}}[B]\{d\}\,\mathrm{d}x\mathrm{d}z + W_{\mathrm{e}} \tag{12}$$

The variational form of the equilibrium equation results from the total energy Π_{P} minimization to the nodal stress and displacement parameters:

$$\begin{cases}\frac{\partial\Pi_{\mathrm{P}}}{\partial\{\sigma\}} = 0\\ \frac{\partial\Pi_{\mathrm{P}}}{\partial\{d\}} = 0\end{cases} \tag{13}$$

where $\{\sigma\}$ and $\{d\}$ are, respectively, the vectors of nodal stresses and displacements degrees of freedom.

After performing the variations to the nodal parameters in (13), the following system of hybrid equations for the finite element is obtained:

$$\begin{bmatrix}[\mathbf{S}_{\sigma\sigma}] & [0] & [\mathbf{S}_{\sigma\mathrm{d}}]\\ [0] & [\mathbf{S}_{\tau\tau}] & [\mathbf{S}_{\tau\mathrm{d}}]\\ [\mathbf{S}_{\sigma\mathrm{d}}]^{\mathrm{T}} & [\mathbf{S}_{\tau\mathrm{d}}]^{\mathrm{T}} & [0]\end{bmatrix}\begin{Bmatrix}\{\sigma_{\mathrm{e}}\}\\ \{\tau_{\mathrm{e}}\}\\ \{d_{\mathrm{e}}\}\end{Bmatrix} = \begin{Bmatrix}\{0\}\\ \{0\}\\ \{F_{\mathrm{e}}\}\end{Bmatrix} \tag{14}$$

where the finite element degrees-of-freedom vectors are defined as

$$\begin{aligned}\{\sigma_{\mathrm{e}}\} &= \{\sigma_{x1}\ \sigma_{x2}\ \sigma_{x3}\ \sigma_{x4}\}^{\mathrm{T}}\\ \{\tau_{\mathrm{e}}\} &= \{\tau_{xz1}\ \tau_{xz2}\ \tau_{xz3}\ \tau_{xz4}\}^{\mathrm{T}}\\ \{d_{\mathrm{e}}\} &= \{w_i\ u_1\ u_2\ w_j\ u_3\ u_4\}^{\mathrm{T}}\end{aligned} \tag{15}$$

In the previous equation, the sub-matrices $[\mathbf{S}_{\sigma\sigma}]$ and $[\mathbf{S}_{\tau\tau}]$ are defined as

$$[\mathbf{S}_{\sigma\sigma}] = D_{\sigma}^{-1}\int_{-L/2}^{L/2}\int_{-h/2}^{h/2}[\mathbf{N}_{\sigma\sigma}(x,z)]^{\mathrm{T}}[\mathbf{N}_{\sigma\sigma}(x,z)]\,\mathrm{d}z\mathrm{d}x \tag{16}$$

$$[\mathbf{S}_{\tau\tau}] = D_{\tau}^{-1}\int_{-L/2}^{L/2}\int_{-h/2}^{h/2}[\mathbf{N}_{\tau\tau}(x,z)]^{\mathrm{T}}[\mathbf{N}_{\tau\tau}(x,z)]\,\mathrm{d}z\mathrm{d}x \tag{17}$$

These two matrices are obtained with exact integration and represent the normal and shear stresses flexibility matrices. The effect of normal stresses on the respective strains participates in Eq. 14 by the matrix defined as

$$[\mathbf{S}_{\sigma\mathrm{d}}] = \int_{-L/2}^{L/2}\int_{-h/2}^{h/2}[\mathbf{N}_{\sigma\sigma}(x,z)]^{\mathrm{T}}\left[\mathbf{B}^{\mathrm{B}}(x,z)\right]\mathrm{d}z\mathrm{d}x \tag{18}$$

This matrix is also obtained from an exact integration calculation.

The complementary work performed by the shear stresses against the shear strains is described by the matrix equation:

$$[\mathbf{S}_{\tau\mathrm{d}}] = \int_{-L/2}^{L/2}\int_{-h/2}^{h/2}[\mathbf{N}_{\tau\tau}(x,z)]^{\mathrm{T}}\left[\mathbf{B}^{\mathrm{S}}(x,z)\right]\mathrm{d}z\mathrm{d}x \tag{19}$$

where matrix $[\mathbf{S}_{\tau\mathrm{d}}]$ is calculated using a reduced integration at point $x = z = 0$.

The global mixed matrix equation is thus described by

$$[\mathbf{S}]\{X_{\mathrm{e}}\} = \{F_{\mathrm{e}}\} \tag{20}$$

where the mixed formulation degrees-of-freedom vector is defined as

$$\{X_{\mathrm{e}}\} = \{\sigma_{x1}\ \sigma_{x2}\ \sigma_{x3}\ \sigma_{x4}\ \tau_{xz1}\ \tau_{xz2}\ \tau_{xz3}\ \tau_{xz4}\ w_i\ u_1\ u_2\ w_j\ u_3\ u_4\}^{\mathrm{T}} \tag{21}$$

The second member of (20) contains the load vector $\{F_{\mathrm{e}}\}$:

$$\{F_e\} = \{0 \cdots 0 \;\; Q_i \;\; F_1 \;\; F_2 \;\; Q_j \;\; F_3 \;\; F_4\}^T \quad (22)$$

where Q_i and Q_j are transverse shear forces acting uniformly along sections $x = -L/2$ and $x = +L/2$, respectively. In addition, $F_{(1\ldots4)}$ are nodal forces along x-direction (instead of normal stresses treated as unknowns) for normal stresses at element nodes.

Condensed displacement-based stiffness matrix

Re-writing Eq. 20 in a compact form as

$$\begin{bmatrix} [\mathbf{S}_{ss}] & [\mathbf{S}_{sd}] \\ [\mathbf{S}_{sd}]^T & [0] \end{bmatrix} \begin{Bmatrix} \{\bar{\sigma}_e\} \\ \{d_e\} \end{Bmatrix} = \begin{Bmatrix} \{0\} \\ \{F_e\} \end{Bmatrix} \quad (23)$$

it is possible to relate the stress field with the displacement field as

$$\{\bar{\sigma}_e\} = -[\mathbf{S}_{ss}]^{-1}[\mathbf{S}_{sd}]\{d_e\} \quad (24)$$

Replacing (24) into the second equation of (23), the condensed form of the equation system is defined as

$$-\left([\mathbf{S}_{sd}]^T[\mathbf{S}_{ss}]^{-1}[\mathbf{S}_{sd}]\right)\{d_e\} = \{F_e\} \quad (25)$$

The inverse of $[\mathbf{S}_{ss}]$ exists, since this matrix is block-diagonal, being defined by

$$[\mathbf{S}_{ss}]^{-1} = \begin{bmatrix} [\mathbf{S}_{\sigma\sigma}]^{-1} & [0] \\ [0] & [\mathbf{S}_{\tau\tau}]^{-1} \end{bmatrix} \quad (26)$$

With the solution discussed herein, the displacement vector $\{d_e\}$ can be calculated from the assembled reduced form (25). The displacement-based solution can then be applied to the original assembled mixed form (14), prescribing additionally the natural shear stresses boundary conditions at the top and bottom faces of the beam, to determine the full stress field.

Mass matrix

The consistent form of the mass matrix can be defined as

$$[\mathbf{M}] = \rho b \int_{-L/2}^{L/2} \int_{-h/2}^{h/2} [\mathbf{N}(x,z)]^T [\mathbf{N}(x,z)] \, dz dx \quad (27)$$

where ρ and b are respectively, the mass density (assuming the material to be homogeneous) and the beam width. The element matrix organization follows the displacement degrees of freedom applied in (15).

Alternatively, the lumped mass matrix of a four-node finite element, as the one hereby formulated to model each layer, presents a diagonal shape where the leading diagonal elements are calculated by distributing the total element mass among the finite element degrees of freedom, as

$$[\mathbf{M}] = \frac{\rho \cdot b}{4} Lh \begin{bmatrix} 2 & & & \cdots & & 0 \\ & 1 & & & & \\ & & 1 & & & \vdots \\ & & & 2 & & \\ & & & & 1 & \\ 0 & & \cdots & & & 1 \end{bmatrix} \quad (28)$$

where L and h are, respectively, the length and the thickness of the four-node element.

Damping model

The sandwich beam is formed by a core made of a low modulus and high loss factor material and two stiff skins which present a relatively high stiffness and insignificant damping characteristics. Therefore, the sandwich finite element model must include a damping operator to represent the damping effect of the material.

Experimental evidence and published studies [18–20] indicate that a frequency dependent hysteretic damping model, usually known as viscoelastic model, can be efficiently used to represent the dissipation mechanism provided by the viscoelastic materials applied in sandwich structures as passive vibration control solutions. A recent study on the composition cork feasibility analysis for sandwich damping solutions [5, 6] showed that these materials evidence a nearly constant storage modulus and loss factor for frequencies above the range of 50–100 Hz (the study results are limited to the frequency range (0–400 Hz). Below this frequency limit, the results obtained revealed a significant dependency of the complex modulus with the frequency, which can be related to the viscous-based dissipation mechanism developed by the cellular structure of the cork and also by the agglomerate macro structure. Therefore, the application of a frequency-dependent viscoelastic model can be effectively used to represent the damping effect of a composition cork.

Similar to the usual viscoelastic materials, the composition cork can be represented by the complex modulus approach, where the strain response to a harmonic imposed stress condition is described by an amplitude ratio, the storage modulus, $E'(\omega)$, and a phase lag, $\delta = \tan^{-1}[\eta(\omega)]$, as

$$\sigma = \bar{E}(\omega)\varepsilon = E'(\omega)(1 + j\eta(\omega))\varepsilon \quad (29)$$

where $\bar{E}(\omega)$ and $\eta(\omega)$ represent, respectively, the complex modulus and the loss factor (ratio between the imaginary part: the loss modulus, and the real part: the storage modulus of the complex modulus parameter). Symbol $j = \sqrt{-1}$ represents the complex operator.

Since the material storage modulus is assumed to be frequency dependent, the stiffness matrix of a layer made from composition cork is thus also frequency dependent.

Since the *Poisson*'s ratio dependency with the frequency is negligible in practice, this material parameter is usually considered frequency independent and constant. Therefore, the stiffness matrix for a damping layer with viscoelastic behaviour can be described as

$$[\mathbf{K}(\omega)] = E'(\omega)[\mathbf{K}_0] \tag{30}$$

where $E'(\omega)$ stands for the storage modulus (real component of the complex modulus) and $[\mathbf{K}_0]$ represents a factorized stiffness matrix for $E'(\omega) = 1$.

The viscoelastic damping model represents the dissipation component of the material, being directly related to the loss modulus of the material. Therefore, the damping matrix is assumed to be proportional to the stiffness matrix, this proportionality being directly defined by the loss factor η, as

$$[\mathbf{H}(\omega)] = \mathrm{j}\eta(\omega)[\mathbf{K}(\omega)] \tag{31}$$

This damping model can be directly introduced in the equation of motion described in the frequency domain, which can be straightforwardly solved using a direct frequency analysis procedure [18] to determine a set of frequency response functions.

Experimental characterization of a composition cork

Cork presents a cellular structure formed by thin-walled prismatic cells oriented along the radial direction of the tree. Figure 2 depicts a scanning electronic microscopy (SEM) image taken from an Axial-Transversal section of a natural cork. Such cellular structure presents a homogeneous distribution of a 4–9-sided polygon-shaped corrugated prismatic cells [8], without intercellular gaps, filled with a gaseous substance similar to air.

A detailed analysis on the cellular structure reveals that the cellular voids represent most of the cork volume, which justifies its low density and most of its unique properties. This distinctive structure seems to be also responsible for the behaviour of the cork under compression and tension, as well as its dynamic characteristics.

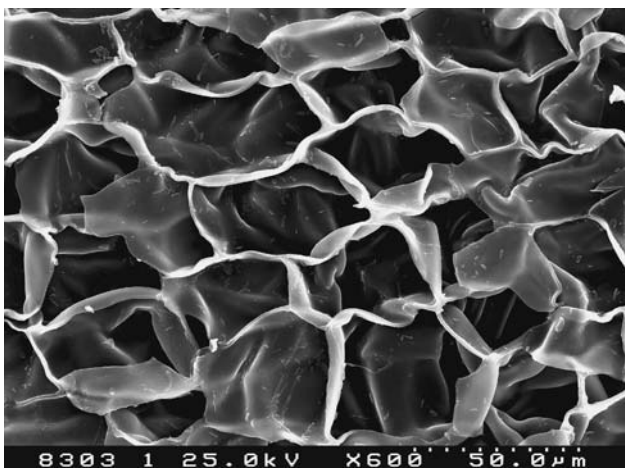

Fig. 2 Scanning electronic microscopy image of natural cork

Static characterization

Compressive test

In order to characterize the static compressive behaviour of the target composition cork, a set of eight small (20 × 20 × 20 mm) specimens were tested in a *Shimadzu* AG-50KNG testing machine using a *Shimadzu* SLBL-5KN load cell and a test velocity of 5, 10 and 20 mm/min. Figure 3 represents a set of different stages during a 2 mm/min compression test on a similar specimen (27 × 26.5 × 20 mm), evidencing not only the remarkable compressive capacity, but also the insignificant transversal deformation, which supports the assumption of a null *Poisson*'s ratio for deformation levels up to 50–70%.

Despite the heterogeneous nature of the cork, the experimental results revealed a homogeneous and isotropic compressive behaviour for specimens taken from the same composition cork plank. The small size of the cork granules and the different orientation that these granules assume inside the agglomerate bulk during transformation process are responsible for this homogenization process.

Figure 4 represents the load–displacement curves obtained for a set of specimens, wherein the usual three compression stages, as described in the literature [8, 11, 14], are clearly identified. The initial stage reveals a nonlinear elastic behaviour, resulting from the elastic bending of the cells walls. This stage is followed by a nearly constant level plateau, evidencing the effects of a progressive buckling of the cells walls. Finally, in the third stage, the cork walls become completely collapsed and the compressive behaviour is predominantly ruled by the wall's material properties. It is worthy to mention that after the compressive test, where a deformation up to 80% was imposed, the specimens recovered almost the initial dimension, presenting a mean residual deformation lower than 7.5%.

The sequence of images depicted in Fig. 3 evidences the relatively reduced lateral deformation of the specimens which, as expected, indicate a reduced value of the material *Poisson*'s ratio. This observation is directly related to the initial and natural wall corrugation presented by the cellular structure of the cork, which also explains the relative significant difference of the material's behaviour under compression and tension loading.

As indicated in the legend of Fig. 4, three different test velocities were used, and the results obtained proved to be independent of this parameter, at least within the velocity range used in this study. In addition, for each constant

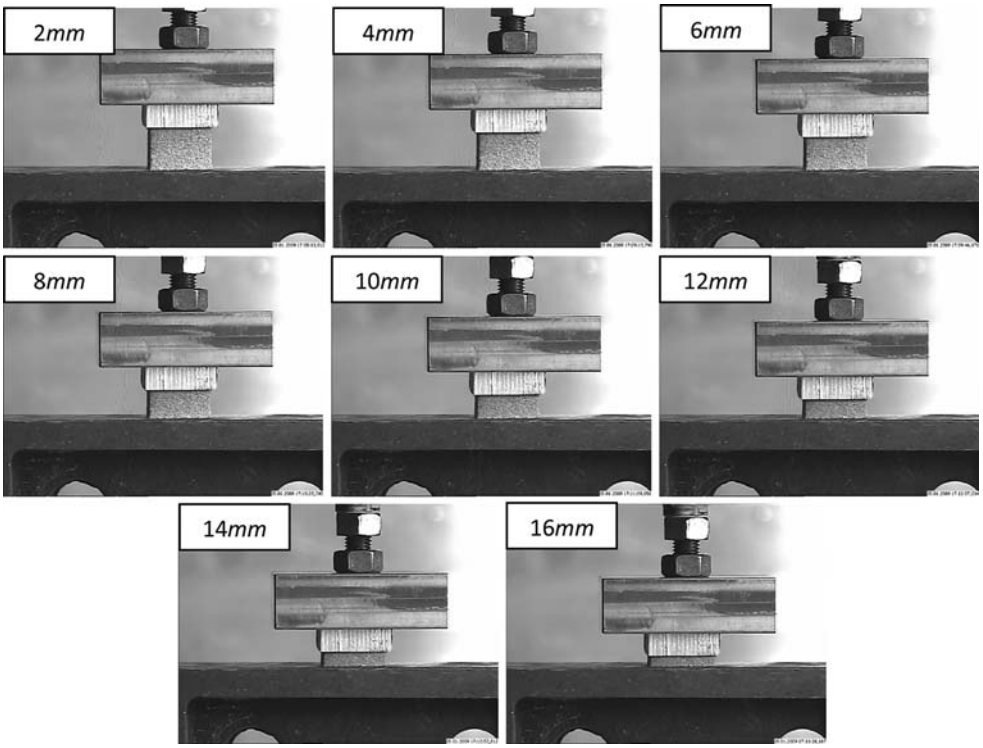

Fig. 3 Composition cork compressive test: visual analysis of deformation pattern

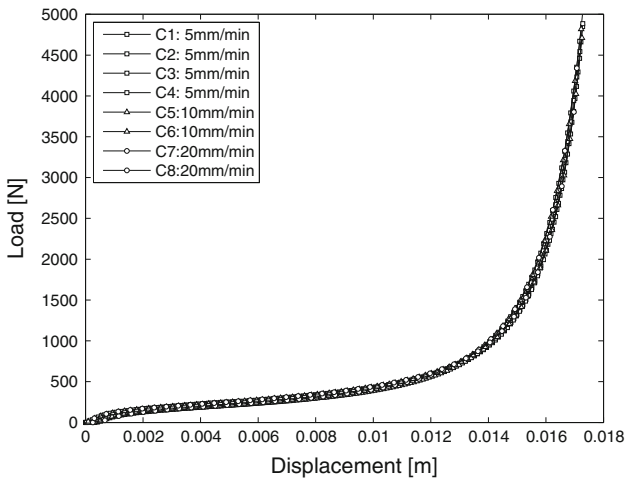

Fig. 4 Compression test displacement–load graph

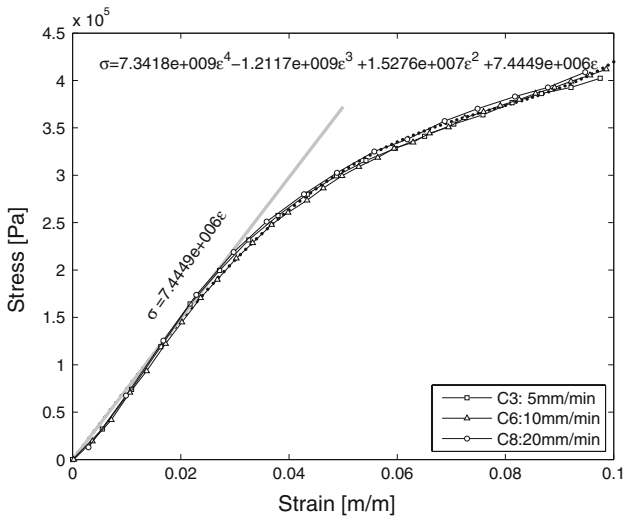

Fig. 5 Compression test stress–strain curve

velocity subset, different orientations of the cubic specimen in relation to the axial loading direction were used to analyse the isotropy characteristics of the material. The stress–strain relation follows the displacement–load graph and, for small deformation levels, the initial deformation stage can be used to describe the composition cork behaviour (Fig. 5). For this particular material, the stress–strain relation was assumed to be represented by a fourth-order polynomial equation (dotted line in Fig. 5) whose parameters were fitted to the experimental stress–strain graph within the low deformation range.

According to the results obtained from this set of specimens, the composition cork herein analysed can be described by a reference compression of *Young*'s modulus of 7.4 MPa (standard deviation: 0.3 MPa).

Tensile test

Using the same equipment and testing conditions as applied in the compressive test, five tensile specimens were tested at a test velocity of 5, 10 and 20 mm/min.

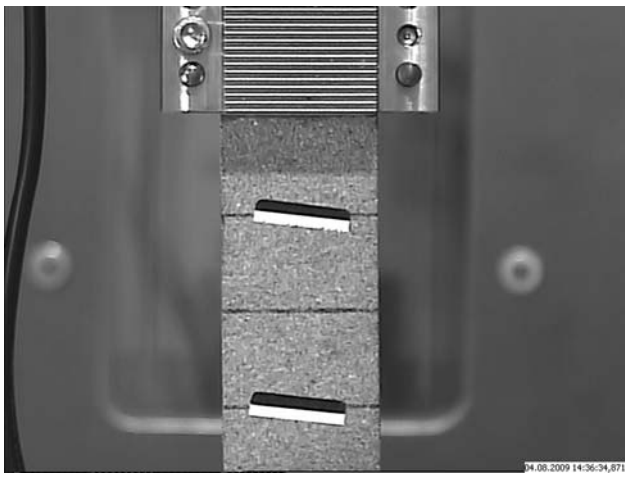

Fig. 6 Composition cork tensile specimen

Fig. 7 Tensile testing setup

The specimen assembly, depicted in Fig. 6, consists of a composition cork bar (40 × 12 mm section) with a set of glued aluminium support plates to reduce the fixture effect and improve the unidirectional stress field.

The specimen was tested in the *Shimadzu* tension machine, as illustrated in Fig. 7, using a video extensometer device (*Messphysik* ME 46NG) to measure the specimen uniaxial deformation.

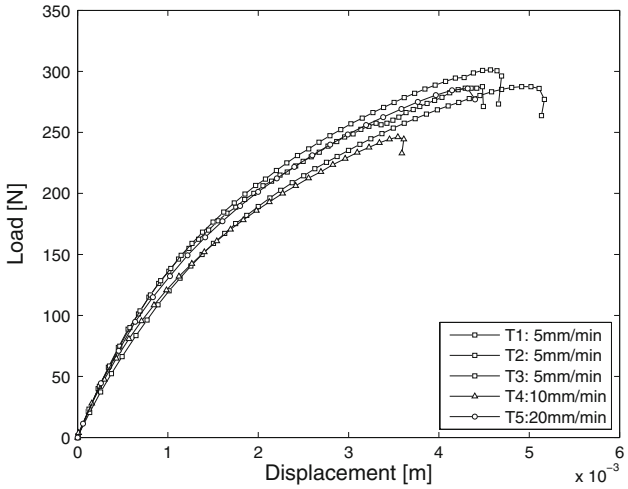

Fig. 8 Tensile testing load–displacement curve

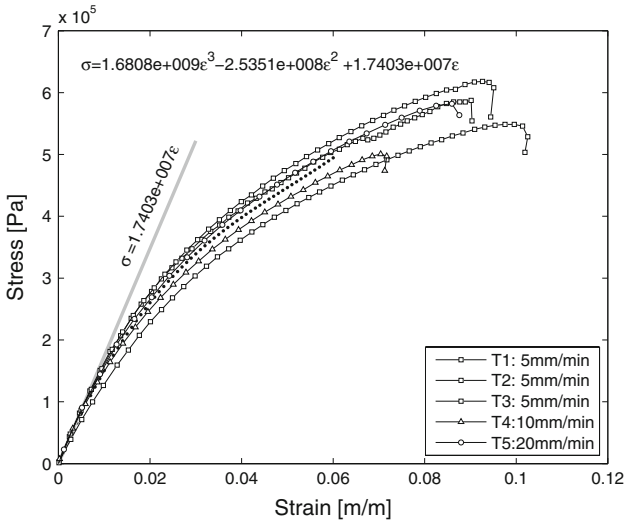

Fig. 9 Tensile test stress–strain curve

Figure 8 represents the load–displacement curves for the analysed tensile specimens whereas Fig. 9 depicts the stress–strain distribution, corresponding mean cubic fit relation (dotted line) and linear stress–strain relation describing the *Young*'s modulus (grey line).

The results obtained, which were satisfactorily correlated, evidenced an initial mean tension modulus of about 17.4 MPa (standard deviation: 1.3 MPa), which is clearly higher than the modulus obtained from the compressive test. This observation is in accordance to the information provided by several researchers [8, 12–14] and, as described before, can be explained by the initial corrugation of the cell wall.

Following the compression test observations, the results obtained from the tensile test also did not show a clear dependence upon the deformation velocity within the limits hereby considered.

Dynamic characterization

Direct identification: semi-definite dynamic system

Considering that the composition cork dynamic behaviour can be described by a frequency-dependent viscoelastic model, a vibration-based testing procedure can be used to identify the material complex modulus. For this purpose, a special experimental setup, representing a semi-definite two degrees-of-freedom dynamic system, can be applied [5]. In this assembly, depicted in Fig. 10, the composition cork sample, representing the complex stiffness of the system, $\bar{K}(\omega)$, is inserted between two translating masses, m_1(100 g) and m_2(3100 g).

An electro-dynamic shaker (*LDS* V400), suspended from an independent rigid frame was used to provide the system random excitation within the 0–400 Hz frequency range. An impedance head (*Brüel&Kjaer* 8200), attached to the moving mass m_1, was used to measure the applied force and moving mass response. The response of mass m_2 was measured using a piezoelectric accelerometer (*Brüel&Kjaer* 4371).

Using both transducers signals, the driving point accelerance function, $A(\omega)$ and the relative transmissibility function, $T(\omega)$ (Fig. 11), were obtained by a spectral analyser (*Brüel&Kjaer* 2035).

These response functions can be directly applied for the determination of the extensional complex modulus function, $\bar{E}(\omega)$, through the relations:

$$\bar{E}(\omega) = \frac{h}{A}\frac{\omega^2 m_2 T(\omega)}{1 - T(\omega)} \tag{32}$$

$$\bar{E}(\omega) = \frac{h}{A}\frac{\omega^2 m_2 (m_1 A(\omega) - 1))}{(m_1 + m_2)A(\omega) - 1} \tag{33}$$

where h and A represent, respectively, the thickness and the cross-sectional area of the composition cork specimen. Figures 12 and 13 represent the identified extensional storage modulus and loss factor functions within the 0–400 Hz frequency range.

Fig. 10 Experimental setup for the semi-definite dynamic system

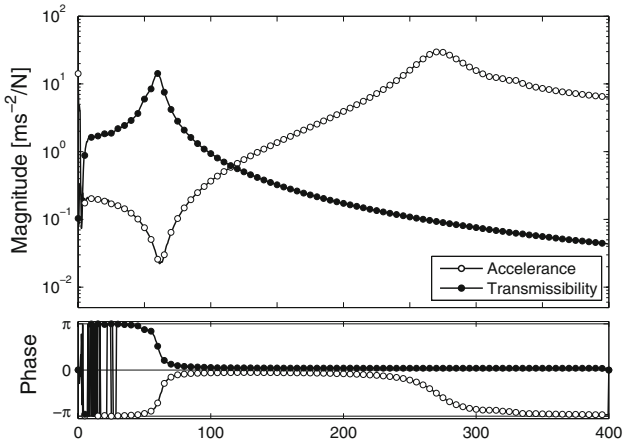

Fig. 11 Frequency response functions: accelerance and transmissibility

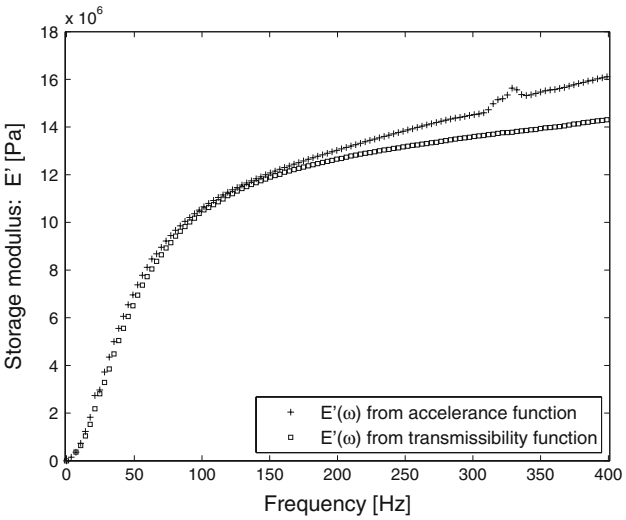

Fig. 12 Storage modulus $E'(\omega)$ for the composition cork sample

Analysing the storage modulus function representation in Fig. 12, it becomes evident that this characterization is not representative of the real material behaviour for the low frequency range; the static modulus within the range between 7.4 MPa (compression) and 17.4 MPa (tension) would be expected to be found. This low frequency discrepancy is readily justified since, in this frequency range, the inertial effect of mass m_2 is not enough to provide a significant deformation of the material specimen and the semi-definite system performs a rigid body motion. Furthermore, the applied small electro-dynamic shaker is also unable to supply the required load intensity for such low frequencies. Therefore, this low frequency data is misrepresentative and should be disregarded.

Concerning the loss factor distribution, depicted in Fig. 13, the assumption of a quasi-constant loss factor around 10% seems to be acceptable.

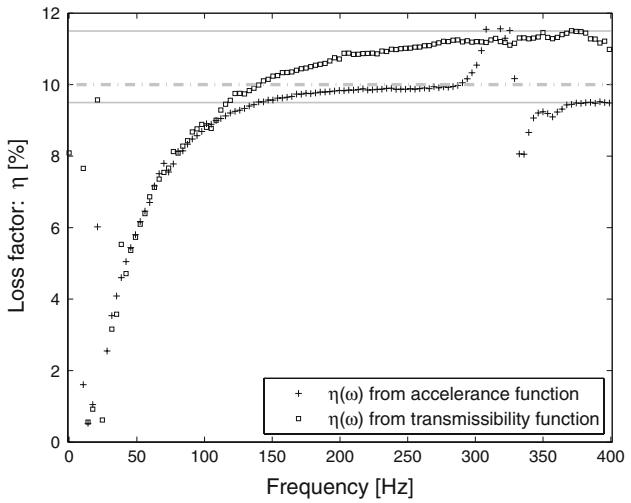

Fig. 13 Loss factor $\eta(\omega)$ for the composition cork sample

Inverse identification: free-vibration based

As an alternative to the direct static and dynamic identification methods previously exposed, it is also possible to infer the properties of the composition cork core material from the static or dynamic response of a sandwich beam (or plate) as long as the skin properties are assumed to be accurately identified. Clamped or three-point bending beam deflection analyses are usual indirect identification methods of single material or composite beams.

In this analysis, the free vibration response of a clamped sandwich beam is applied to identify the storage modulus and loss factor for the fundamental frequency of the beam. Therefore, to identify the low frequency storage modulus, incorrectly described in Fig. 12, two sandwich beams, beam CA and beam CB, were manufactured using two identical pairs of 1050 aluminium alloy skins (498 × 30 × 2 mm). The composition cork applied in the beam specimens was taken from the same plank used for the material characterization study, from which two pieces of 433 × 30 mm, with a thickness of 6.3 mm (beam CA) and 9.3 mm (beam CB), were cut using a high speed saw. Table 1 presents the aluminium material properties as well as the assumed or experimentally determined properties for the composition cork material.

A stiff epoxy adhesive was used to assemble the beams, and special care was taken to ensure the homogeneous distribution of the glue along the interface, while minimizing the adhesive layer thickness. In order to improve the clamping boundary condition, an aluminium block with the same thickness and width of the core was also glued to form the clamped root of the beam, as depicted in Fig. 14.

Table 1 Material properties used in the numerical model

Material	*Young*'s modulus	*Poisson*'s ratio	Density (kg m^{-3})
Aluminium	70 GPa	0.32	2710
Composition cork (Ref. 8003)	To be determined	0.0	205

The beam was fixed by using a special fixture applied onto a rigid breadboard (Fig. 15) leaving a free length of 433 mm. An optical fibber displacement transducer (*MTI* KD-300) was applied to measure the tip response to a prescribed 2-mm tip displacement. The signal conditioning and analysis was performed in a spectral analyser (*DSPT* Siglab 2042).

In order to simulate the test conditions, the time–domain response of the beam, considering as the initial conditions the prescribed displacement field, was obtained using the proposed finite element and a direct integration *Newmark* algorithm with an equivalent viscous damping matrix. A 30-beam finite element mesh, with 3 numerical layers, was used.

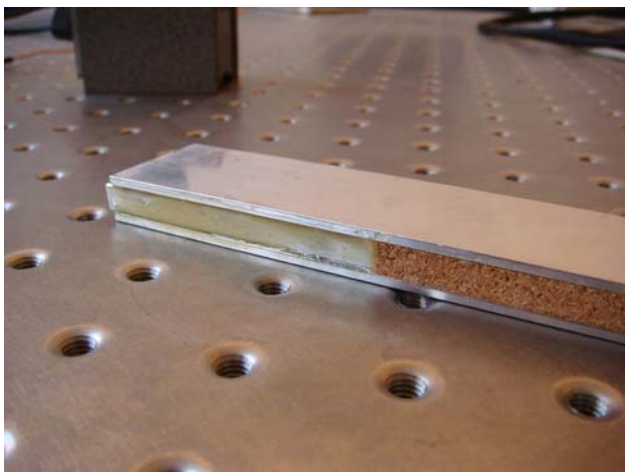

Fig. 14 Detail on the cantilever beam root

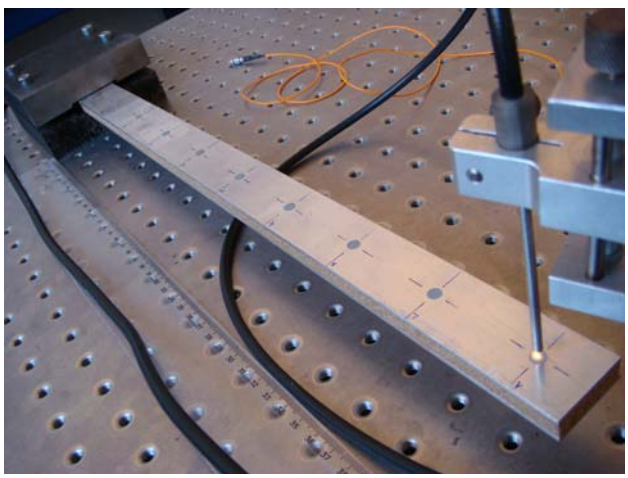

Fig. 15 Free vibration test experimental setup

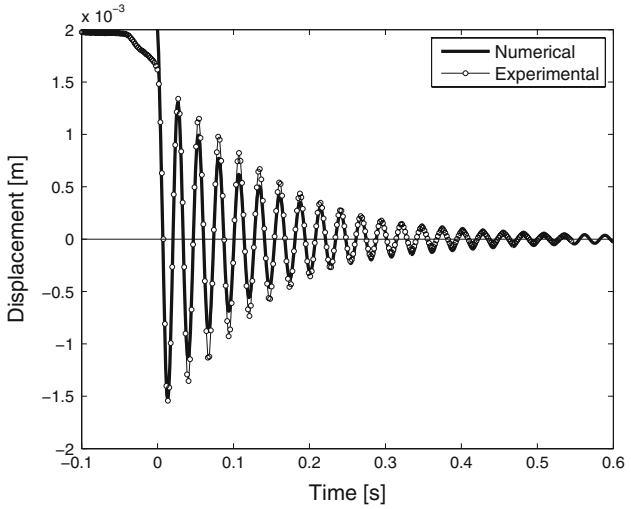

Fig. 16 Time–domain displacement response at the beam tip: beam CA

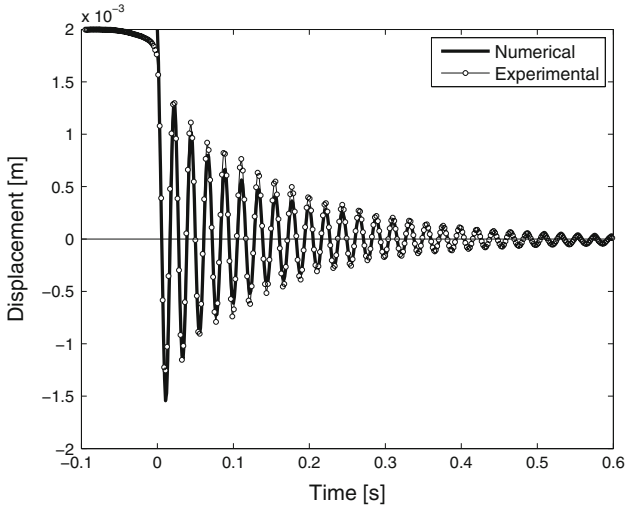

Fig. 17 Time–domain displacement response at the beam tip: beam CB

Figures 16 and 17 represent the experimental and numerical time–domain responses for beam CA and beam CB, respectively.

In order to correlate the experimental and the numerical results, a storage modulus of 12.0 MPa for the composition cork was applied for beam CA and 14.2 MPa for beam CB, with a fundamental natural frequency of, respectively, 37 and 46 Hz. These storage modulus values, which were also validated in a modal analysis procedure, clearly differ from those represented by the complex modulus curve obtained in the electro-dynamic shaker random dynamic test (Fig. 12), as expected, but agree with the static values range defined from the compression and tension static tests results, respectively, 7.4 and 17.4 MPa.

The composition cork density (205 kg/m^3) was identified by weight/volume relation according to standard NP 2372, using several specimens taken from the same raw material plank. The material loss factor was determined by adjusting the corresponding numerical parameter towards a correlation of the numerical curve to the envelope decay of the experimental response. A common value for both specimens of 10% was thus determined, which agrees with the results presented in Fig. 13.

In order to cover the entire frequency range under analysis, the application of the described methodology on several sandwich beams with different free lengths and core/skin thickness ratios would be required. The following method intends to reduce such experimental effort.

Inverse identification: FRF based

Contrary to the previous identification method, which can only describe the core material dynamic modulus for the first natural frequency of the beam, it is possible to identify the same properties for a broad frequency range from an available frequency response function measured experimentally, by using a representative analytical or numerical model in an inverse procedure by adjusting the model properties to fit the measured data.

When dealing with sandwich beams with viscoelastic material cores, the *Ross–Kerwin–Ungar* (RKU) equations [27] were often considered a valuable solution to identify the core material's complex modulus. However, the success of such methodology is usually compromised by the limiting assumptions of the kinematic model on which the identification procedure is based. In order to overcome these limitations, numerical models, usually finite element based, are being currently applied in an iterative optimization procedure. Moreira and de-Carvalho [28] used a beam finite element model to identify a composition cork introduced inside a beam similar to those herein studied.

In order to carry out this identification procedure, two sandwich beams, beam FA and FB (Fig. 18), with the same dimensions of those used in the clamped free vibration test, were freely suspended from a stiff rig to obtain free boundary conditions.

The sandwich beams were manufactured using the same materials and methodology adopted for the clamped beams CA and CB. In this case, the core has exactly the same length of the skins (498 mm of length). Moreover, since the core of each beam was taken from the same material slice used for the clamped beams, these beams have exactly the same thicknesses as the homologous clamped beams, i.e., 6.3 mm for beam FA and 9.3 mm for beam FB. The same epoxy adhesive and bonding methodology were used to assemble the beams. An equally spaced measurement mesh of 11 points was considered for each beam.

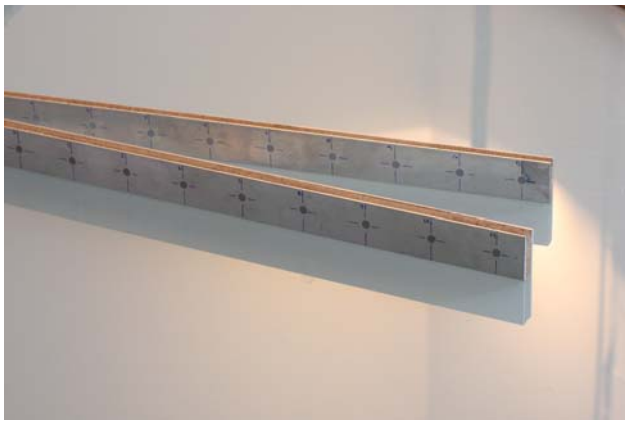

Fig. 18 Free sandwich beams: beam FA and beam FB

An electro-dynamic shaker (*LDS* 201) was used to apply a 0–500 Hz random excitation at point 4 of the beam, and the excitation force was measured with a miniature force transducer (*Brüel&Kjaer* 8203). In order to measure the beam response at each of the 11 points of the measuring mesh, a laser vibrometer (*Polytec* OFV303) was employed (Fig. 19). A spectral dynamic analyser (*Brüel&Kjaer* 2035) was used for the signal conditioning and analysis, and calculation of the frequency response functions.

The numerical identification procedure is based on a minimization scheme wherein the numerical model and the associated material properties are iteratively updated. This optimization procedure is driven by a correlation analysis between the numerically generated frequency response model and the experimental frequency response function (FRF). More details on this procedure can be found in [28]. In this case, only the storage extensional modulus $E'(\omega)$ and the loss factor $\eta(\omega)$ constant functions for the composition cork were considered as optimization parameters,

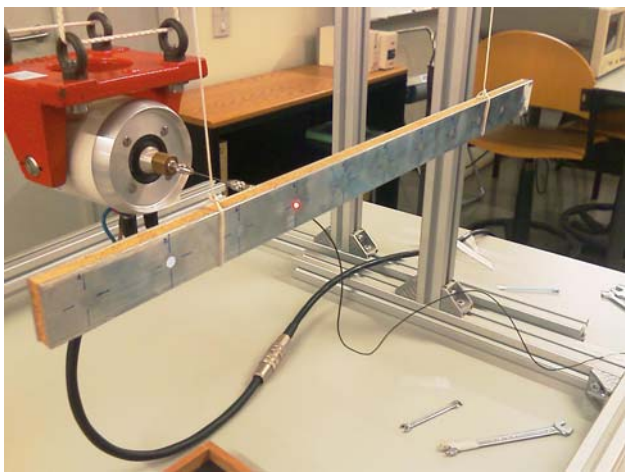

Fig. 19 Experimental setup for the free sandwich beam vibration analysis

representing the *Poisson*'s ratio and the material density as $\nu = 0.0$ and $\rho = 205$ kg/m^3, respectively.

In order to prove the validity of the fitting approach and the obtained results, the composition cork properties were identified considering the beam FA experimental data, and then the identified properties were used to generate the numerical frequency response model of the beam FB.

The graphical representation depicted in Fig. 20 overlaps the fitted numerical driving point FRF on the corresponding experimental FRF. Figure 21 shows the Frequency Response Assurance Criterion (FRAC) [29, 30] herein applied as the correlation indicator driving the fitting process. The identified properties are storage modulus $E'(\omega) = 20.8$ MPa and loss factor $\eta = 10.6\%$.

Figure 22 represents the numerical and experimental driving point frequency response functions for the thicker beam (beam FB), using the identified material properties in the numerical model. As evidenced by the graphical agreement as depicted in Fig. 22 and by the correlation indicator distribution represented in Fig. 23, there is a good correlation level between the experimental data and the numerically generated frequency response model for the

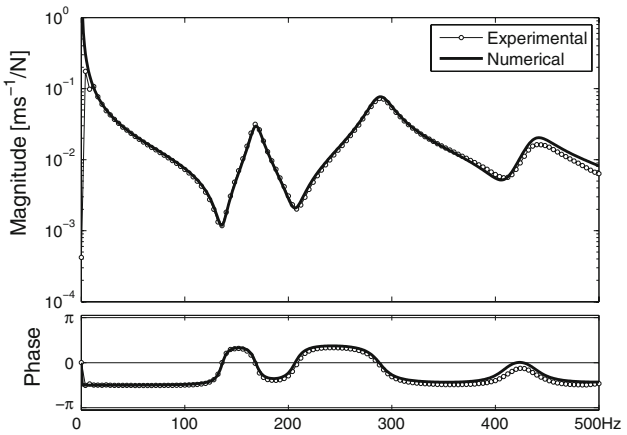

Fig. 20 Driving point frequency response functions for beam FA

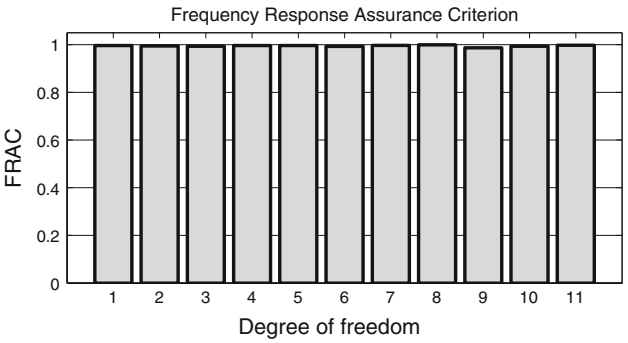

Fig. 21 Frequency response assurance criterion (FRAC) for beam FA

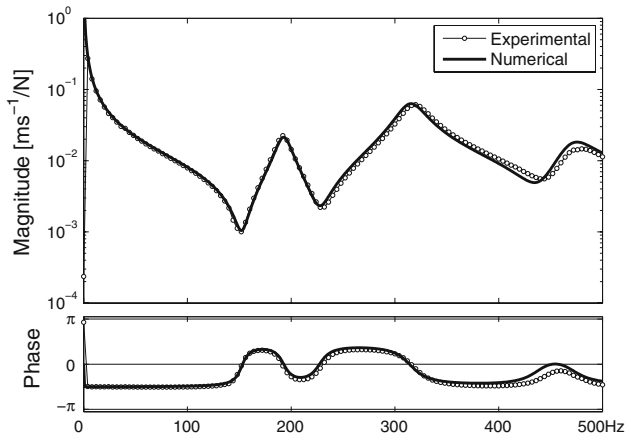

Fig. 22 Driving point frequency response functions for beam FB

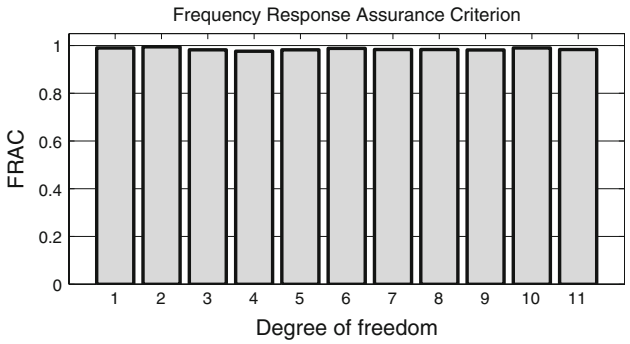

Fig. 23 Frequency response assurance criterion (FRAC) for beam FB

entire set of selected degrees of freedom corresponding to the lateral displacements.

Characterization data analysis

In order to analyse and compare the results obtained from the various characterization methodologies adopted and discussed before, Fig. 24 gathers the previously identified *Young*'s modulus (from the static characterization) and extensional storage modulus (from the dynamic characterization) results.

As shown in the graphical representation in Fig. 24, there is some discrepancy on the results obtained. Nevertheless, and taking into consideration the remarks on the results obtained from the discrete system dynamic characterization procedure, it is possible to observe that the *Young*'s modulus is different for compression and tensile deformation. This observation, which was previously described and justified, agrees with the results and the cellular analysis presented in the literature.

On the other hand, the storage modulus results evidence the difficulties of this characterization procedure. As discussed before, the characterization methodology based on the discrete system has some limitations which may

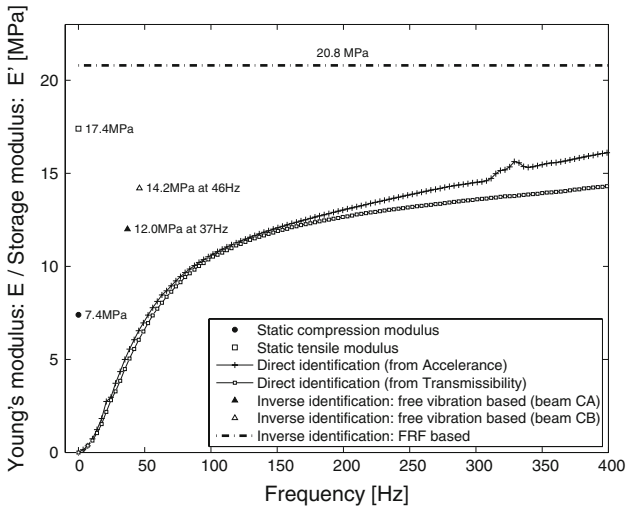

Fig. 24 Global representation of the obtained results

compromise the accuracy of the obtained results, namely the low frequency limitations of the effective load conditions. The procedure based on the analysis of the free vibration response of a cantilever sandwich beam has potentially the effects of the clamping conditions which may affect especially the low frequency natural modes. However, the results obtained agree with those obtained from the static characterization, although being slightly lower than expected, considering the static results.

Finally, the storage modulus constant function identified through the inverse method is slightly higher than the storage modulus results obtained from the direct method using the discrete system dynamic response and the single frequency results identified from the free vibration response of clamped sandwich beams. Nevertheless, despite the slight difference of the obtained results, these present the same order of magnitude and may provide a confidence range for the *Young*'s modulus and extensional storage modulus for this specific composition cork.

Experimental and numerical analysis of composition cork sandwich beams

In order to validate the material characterization, a set of experimental studies were performed on the sandwich beams with composition cork cores used in the characterization study, adopting, however, different boundary conditions. For this purpose, a three-point bending test was used to evaluate the static characterization of the composition cork. In addition, in order to clarify the validity of the results obtained from the dynamic characterization of the material's storage modulus, a set of two cantilever sandwich beams were employed in a frequency response analysis.

Three-point bending test

The two sandwich beams FA and FB were tested in a three-point bending test configuration. Figure 25 presents the test setup, where the same equipment and testing conditions as applied in the composition cork characterization was used. In addition, a *Messphysik* ME 46 NG video-extensometer was applied to measure the displacement of the midpoint of the bottom skin. The beam was placed on two rigid rollers, leaving a free span of 460 mm between the supports.

The numerical model was then used to simulate the three-point test, using the composition cork material properties obtained from the static tests conducted along this study. An 8-layered, 40-finite-element model was applied, using six layers to represent the core.

Figure 26 represents the experimental displacement–load curves for both beams, beam FA and beam FB. The numerical linear elastic results were obtained considering an equivalent *Young*'s modulus of 12.4 MPa calculated as a mean value of the static results: 7.4 MPa (from the compression test) and 17.4 MPa (from the tensile test). The remaining material properties are identical to those previously presented in Table 1.

As observed from the numerical and experimental results, the identified initial static mean modulus of 12.4 MPa can effectively be used as an initial value for this specific composition cork. Nevertheless, for higher load conditions, the load–displacement curve starts to evidence the nonlinear geometric effects, besides the nonlinear material behaviour clearly shown by the material during the static compression and tensile tests.

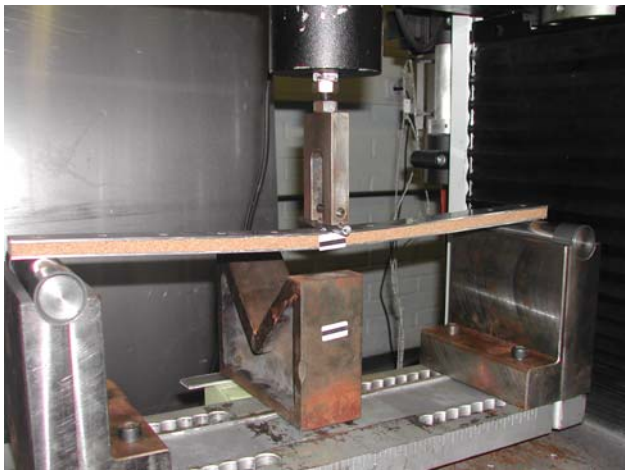

Fig. 25 Three-point bending test setup

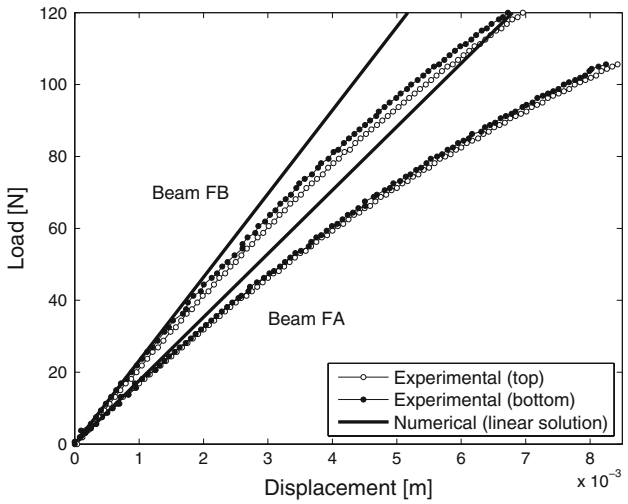

Fig. 26 Experimental and numerical results for the three-point bending test

Frequency response analysis

In order to verify and conclude on the validity of the extensional storage modulus results obtained from the three characterization methods herein applied, the clamped beams CA and CB were used in an experimental study to obtain a set of frequency response functions. These experimental FRFs are then correlated with the numerical results using the identified storage modulus.

Nine equally spaced points are defined at each beam and an instrumented impact hammer (*Kistler* 9722A2000, impact tip 9904A) was used to provide the excitation inside the frequency band of the analysis [0–500] Hz. In order to measure the beam response, a lightweight miniature accelerometer (*Dytran* 3225F) was applied. A spectral analyser (*DSPT* Siglab 2042) was used for the signal acquisition and conditioning, providing the experimental accelerance FRFs. Figure 27 depicts the experimental setup used in this study.

Using the proposed finite element, a set of frequency response functions was calculated. The aluminium material

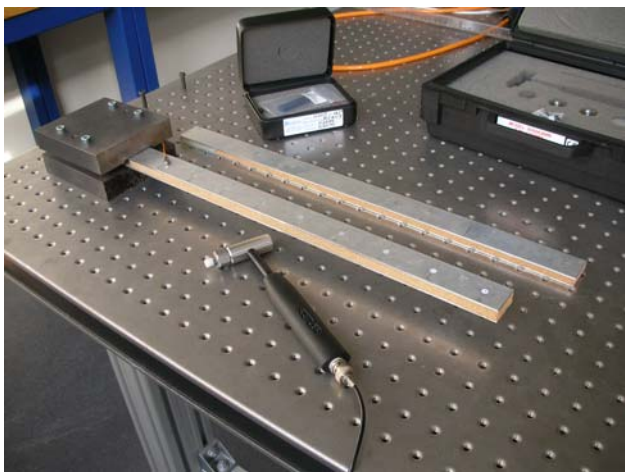

Fig. 27 Experimental setup for the clamped sandwich beam vibration test

properties are identical to those presented in Table 1. For the core material's storage modulus, a constant value of 20.8 MPa, as determined from the inverse method, and a value of 12 and 14.2 MPa, as determined from the free vibration test for beam CA and CB, respectively, was used to assess the characterization results described along the previous section.

Figures 28 and 29 compare the experimental driving point FRF with the numerical results for beam CA and CB, respectively. As shown by these graphical representations, as well by the remaining results obtained for the entire set of analysed degrees of freedom, the numerical results using the low frequency storage modulus, identified from the clamped beam free response method, evidence a good correlation level in the vicinity of the fundamental natural frequency but are clearly uncorrelated for the frequency band above this range. On the other hand, when using the higher constant storage modulus value identified from the inverse methodology, the numerical results agree well with the experimental FRFs, especially within this higher frequency range. These observations, which are valid for both specimens, suggest a non-constant storage modulus function with a frequency distribution following the results obtained from the characterization method on the discrete dynamic system (Fig. 12).

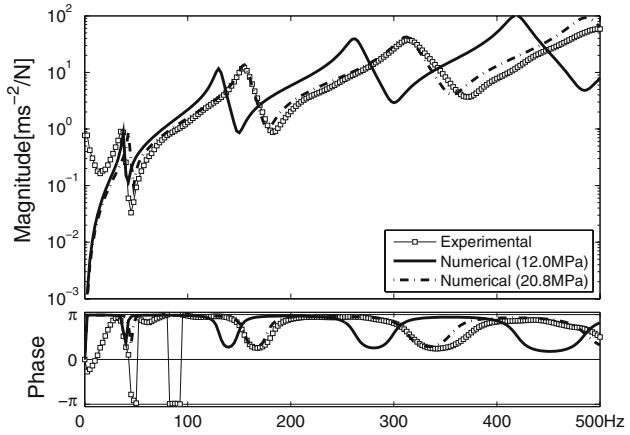

Fig. 28 Experimental and numerical frequency response model for beam CA

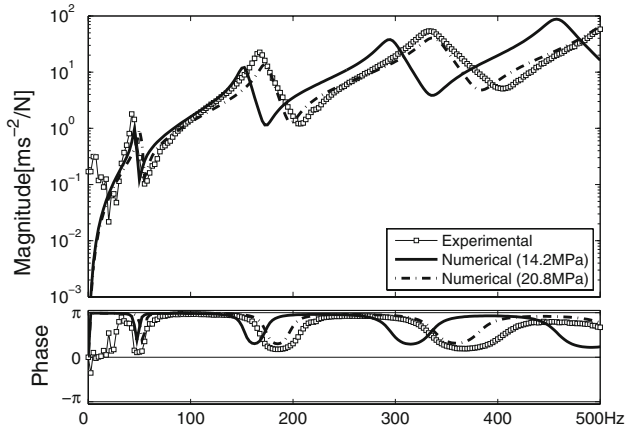

Fig. 29 Experimental and numerical frequency response model for beam CB

Analysing the mobility functions used in the inverse identification method (Figs. 20 and 22), in comparison to the FRFs of the clamped beams (Figs. 28 and 29), it becomes clear that the fitted model from the inverse identification is preponderantly ruled by the high frequency contents of the FRFs. Therefore, the validity of the identified constant modulus value may be limited to the medium/high frequency band and may misrepresent the real material's behaviour for the low frequency range. This observation is perfectly validated when analysing the frequency response correlation indicator, the FRAC function, as depicted in Figs. 30 and 31.

In Figs. 30 and 31, the darker bars (indicated as *b*) represent the FRAC results when comparing the experimental data with the numerical results considering a constant storage modulus of 20.8 MPa. This correlation indicator was calculated considering the entire set of FRFs, for the nine measured degrees of freedom, but does not consider the low frequency range (<100 Hz). On the other hand, the lighter bars (indicated as *a*) are related to the correlation indicator between the experimental data and the

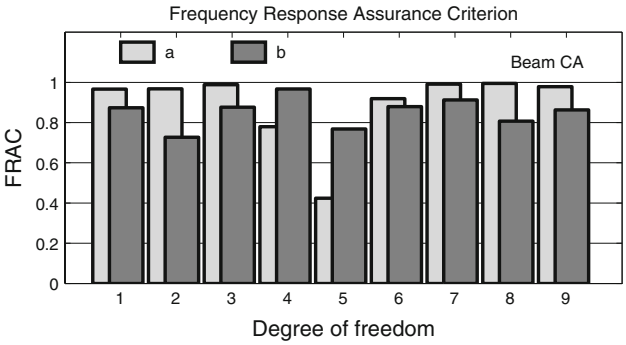

Fig. 30 Frequency response correlation indicator for beam CA

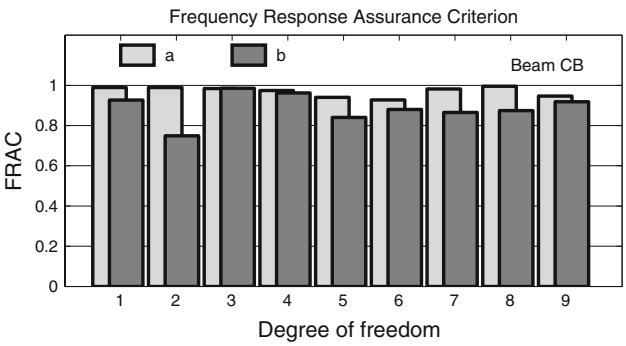

Fig. 31 Frequency response correlation indicator for beam CB

numerical results for the low frequency storage modulus, identified from the free vibration analysis on these clamped beams (12 and 14.2 MPa). The correlation results are restricted to a narrow frequency range centred at the fundamental natural frequency of each beam. It is worthy to mention that the relatively lower correlation indicator for beam CA for the low frequency results is primarily caused by the effects of free body modes of the experimental setup on the measured set of FRFs (clamping assembly is mounted on a stiff optical breadboard supported by rubber pads).

Based on the correlation indicators, it can be concluded that the storage modulus shall be described by a frequency dependent function, especially for the low frequency range. Nevertheless, it seems to be plausible to assume that, for higher frequencies, the storage modulus function has a horizontal asymptote, where a constant value can be used without a major loss of accuracy.

Conclusions

This study presents a comparative analysis of several methodologies for experimental characterization of the static and dynamic properties of composition corks for vibration damping applications. In addition, an efficient beam finite element model based on a mixed formulation is proposed, implemented and applied as a valuable tool for inverse identification methodologies, to verify the results obtained and thus assess the different characterization methodologies.

Concerning the static modulus, i.e., *Young*'s modulus, the results obtained are in perfect accordance to the usual behaviour of a cellular material and can be compared to those values presented in the literature for other composition corks and natural corks. The micromechanics of the cellular structure is the major responsible for the observed behaviour of the cork specimens under compression or tensile loading. The results obtained from the static characterization procedures shall be regarded with confidence, as experimentally and numerically assessed in this study.

While common polymeric-based damping materials are straightforwardly described by a frequency-dependent hysteretic model, or viscoelastic model, the cellular structure of the cork observed from SEM images suggests a significant contribution of a viscous damping mechanism onto the dynamic behaviour of the composition cork, with special relevance at the low frequency range. In fact, the experimental results provide some evidences of this behaviour for low frequencies, both in terms of the storage modulus and loss factor. This behaviour suggests that the gaseous substance trapped inside each cork's cell acts as an air spring with significant effect for low frequencies.

For higher frequencies, and inherently lower levels of deformation, the air spring and the viscous damping effects lose significance, while the effect of the viscoelastic nature of the cell wall's material becomes more important and rules the dynamic behaviour of the composition cork. Furthermore, for the higher frequency range, the polymeric-based adhesive used as binding agent evidences its viscoelastic nature. Nevertheless, SEM analysis onto the interface region between adjacent cork grains show that the amount of binding agent is minimal, which may reduce the effect of this added component onto the composition cork behaviour.

While the loss factor results obtained from the different characterization strategies are consistent, and indicate a constant mean value of 10% for the frequency range herein considered, the storage modulus results present some discrepancy (frequency-dependent function ranging from 12 to 21 MPa) but the values obtained have the same order of magnitude and provide a confidence interval describing the storage modulus for the studied composition cork.

The proposed finite element proved to be accurate and valuable for the simulation of multilayer sandwich beams with high stiffness ratios. The mixed formulation allows to directly impose the displacement and stress fields continuity conditions at the layer's interface, as well as to prescribe the free face stress field conditions.

Acknowledgements The authors gratefully acknowledge the Fundação para a Ciência e a Tecnologia (FCT) of the Ministério da Ciência e da Tecnologia of Portugal for the financial supported under the research project PTDC/EME-PME/66741/2006. Authors also acknowledge Corticeira Amorim Indústria SA company for providing the composition cork used in this study.

Appendix: Composition cork description

Manufacturer's specification:

Manufacturer:	ACC—Amorim Cork Composite (Portugal)
Material reference:	CAI 8003
Binding agent:	Polyurethane
Grain size:	Small (size range: 0.5–1.0 mm)
Grain density:	Low density
Specific weight:	170–240 kg/m^3

References

1. Nashif AD, Jones DIG, Henderson JP (1985) Vibration damping, 1st edn. John Wiley & Sons, New York
2. Jones DIG (2001) Handbook of viscoelastic vibration damping, 1st edn. John Wiley & Sons, New York

3. Moreira RAS, Dias Rodrigues J (2006) Int J Struct Stab Dyn 6(3):397
4. Moreira RAS, Dias Rodrigues J (2010) J Sandwich Struct Mater 12:181
5. Santos Silva J, Moreira RAS, Dias Rodrigues J (2010) J Sandwich Struct Mater. doi:10.1177/1099636209104538
6. Dias Rodrigues J, Moreira RAS (2007) Sandwich structures with cork compound layers: a new vibration control solution. POCI/EME/61967/2004 Final Report, FEUP/UA
7. Gibson LJ, Easterling KE, Ashby MF (1981) Proc R Soc Lond A 337:99
8. Fortes MA, Rosa ME, Pereira H (2004) A cortiça. IST Press, Lisboa
9. Gibson LJ, Ashby MF (1997) Cellular solids, 2nd edn. Cambridge University Press, Cambridge
10. Mano JF (2002) J Mater Sci 37:257. doi:10.1023/A:1013635809035
11. Pereira H (2007) Cork: biology, production and uses, 1st edn. Elsevier, Amsterdam
12. Castro O, Silva JM, Devezas T, Silva A, Gil L (2010) Mater Des 31(1):425
13. Silva SP, Sabino MA, Fernandes EM, Correlo VM, Boesel LF, Reis RL (2005) Int Mater Rev 50(6):345
14. Anjos O, Pereira H, Rosa ME (2006) II Latin American IUFRO Congress, La Serena, Chile, October 23–27, 2006 (In Cd Rom)
15. Giunchi A, Versari A, Parpinello GP, Galassi S (2008) J Food Eng 88(4):576
16. Gil L (2009) Materials 2:776
17. Reis L, Silva A (2009) J Sandwich Struct Mater 11(6):487
18. Moreira RAS, Dias Rodrigues J (2004) J Vib Control 10(4):575
19. Moreira RAS, Dias Rodrigues J, And Ferreira AJM (2006) Comput Mech 37(5):426
20. Moreira RAS, Dias Rodrigues J (2006) Comput Struct 84(19–20):1256
21. Moreira RAS, Dias Rodrigues J (2010) Compos Struct 92:201
22. Auricchio F, Sacco H (1999) Int J Numer Methods Eng 44(10):1481
23. Hughes TJR (1987) The Finite Element Method: linear static and dynamic finite element analysis, 1st edn. Prentice-Hall, New Jersey
24. Cook RD, Malkus DS, Plesha ME (1989) Concept and applications of finite element analysis, 3rd edn. John Wiley & Sons (International Edition)
25. Piam THH, Sze K-Y (2001) Adv Struct Eng 4(1):13
26. Brezzi F, Fortin M (1991) Mixed and hybrid finite element methods. Springer-Verlag, New York
27. Ross D, Ungar EE, Kerwin EM Jr (1959) Damping of plate flexural vibrations by means of viscoelastic laminae, Structural Damping. ASME Publication, New York, p 49
28. Moreira RAS, de-Carvalho R (2009) Int J Mater Eng Innov 1(2):254
29. Zang C, Grafe H, Imregun M (2001) Mech Syst Signal Process 15(1):139
30. Pascual R, Golinval JC, Razeto M (1997) Proceedings of the 15th Int. Modal Analysis Conference (IMAC XV), Orlando, FL, USA, p 587